The International Journal of Advanced Manufacturing Technology (2026) 143:1679–1693
https://doi.org/10.1007/s00170-026-17644-2

ORIGINAL ARTICLE

Post-processing-induced improvements in the bending behavior of SLM-produced Ti6Al4V alloy

Sinan Önder[1] · Nurşen Saklakoğlu[2] · Ahmet Sever[3] · Gökhan Başar[4]

Received: 8 May 2025 / Accepted: 31 January 2026 / Published online: 17 February 2026
© The Author(s) 2026

Abstract
This study presents a multiscale evaluation of the effects of various post-processing strategies, including machining, shot peening (SP), and heat treatment, on the static bending behavior of Ti6Al4V alloy produced by selective laser melting (SLM). Five specimen groups were prepared: as-built, milled, milled followed by traditional SP, milled followed by dual SP, and annealed before milling. To establish a detailed structure–property relationship, the study integrates surface roughness measurements, microstructural and fracture surface characterizations with three-point bending tests. Milling significantly improved surface quality, reducing the average surface roughness (R_a) from 17.05 µm in the as-built specimens to 0.43 µm in the only machined ones. This significant reduction contributed to higher bending strength and bending strain compared with the as-built specimens. While conventional SP slightly increased the surface roughness amplitude (R_a, R_z, and R_c), the secondary SP with smaller-diameter shots reduced roughness amplitude again and resulted in a more homogeneous surface topography. Machining alone improved bending strength by 23%, whereas dual SP yielded the highest strength with a 34% increase relative to the as-built specimens, due to induced compressive residual stresses, martensitic α′ lath refinement, reduced surface roughness, and higher dislocation density. Heat treatment transformed the martensitic α′ phase in prior β grains into an α+β structure, and the annealed and machined specimens exhibited a 264% increase in bending strain relative to the as-built specimens and 184% compared to the only machined specimens, with ductility enhancement primarily governed by the α+β transformation and supported by reduced surface roughness.

Keywords Selective laser melting · Ti6Al4V · Multiscale characterization · Process–structure–property relationship · Post-processing · Three-point bending

1 Introduction

Additive manufacturing (AM) technologies, particularly selective laser melting (SLM), have garnered significant attention in recent years due to their capability to produce geometrically complex metallic components with high material efficiency. Among these, SLM stands out as a laser-based powder bed fusion process in which a high-energy laser selectively melts layers of metallic powder according to a predefined digital model. This layer-by-layer fabrication strategy offers numerous advantages over conventional subtractive manufacturing techniques, including reduced material waste, increased design freedom, and the ability to fabricate lightweight lattice structures [1, 2].

Ti6Al4V, an α + β titanium alloy, is one of the most widely used materials in the aerospace, biomedical, and automotive industries owing to its high strength-to-weight ratio, excellent corrosion resistance, and biocompatibility. The microstructural characteristics of Ti6Al4V alloy produced by SLM exhibit significant differences compared to those obtained through conventional manufacturing methods. These differences primarily arise from the unique thermomechanical conditions inherent to the SLM process

✉ Sinan Önder
sinan.onder@deu.edu.tr

[1] Department of Machinery and Metal Technologies, Torbalı Vocational School, Dokuz Eylul University, İzmir 35860, Türkiye

[2] Department of Mechanical Engineering, Celal Bayar University, Manisa 45140, Türkiye

[3] R&D Center, ERMAKSAN Makine Sanayi ve Ticaret A.Ş., OSB, Nilüfer, Bursa 16065, Türkiye

[4] Department of Industrial Engineering, Osmaniye Korkut Ata University, Osmaniye 80000, Türkiye

[3, 4]. Specifically, the SLM technique is characterized by extremely high thermal gradients (up to 10^6 K/m), exceptionally rapid cooling rates (which can reach up to 10^8 K/s), and repeated heating and cooling cycles [5]. As a result of these high cooling rates, the microstructure of the fabricated alloy is composed of a significant amount of martensitic α′ phase formed within the prior β grains [6, 7]. The presence of metastable α′ phase, ultrafine grain sizes, and a high density of dislocations imparts the material with high strength and hardness. However, these same features adversely affect ductility, typically limiting the elongation to a range of 2–7% [8]. To mitigate these drawbacks, various post-processing methods such as hot isostatic pressing (HIP), machining, heat treatment, and shot peening (SP) are widely employed. These processes aim to reduce residual stresses, decrease porosity, improve surface quality, and modify the microstructure, thereby enhancing the mechanical performance and reliability of components manufactured by SLM [1, 9–11].

Although numerous studies have investigated the effects of various post-processing treatments on the mechanical properties, microstructure, and surface roughness of SLMed Ti6Al4V alloy, studies specifically focusing on the influence of post-processes on bending behavior remain quite limited. Bending loads are among the most commonly encountered stress types in service conditions of components such as aircraft engines, biomedical implants, and structural supports. Therefore, understanding how different post-processing techniques affect the bending behavior is of great importance for real-world application scenarios. In the study conducted by Wu and Lai [12], three-point bending specimens of SLM-produced Ti6Al4V were fabricated in both vertical and horizontal orientations and tested under as-built and HIPed conditions. After the application of the HIP process, the vertically built specimens recorded a 37% increase in bending strength. In the study conducted by Yeşilkaya et al. [13], the effects of different process parameters and two heat treatments on the bending behavior of Ti6Al4V specimens produced by the direct metal laser sintering (DMLS) method were investigated. It was reported that, at a constant laser power, bending strength tended to increase as the hatch spacing decreased. Additionally, the specimens subjected to heat treatment involving holding at 790 °C for 1 h, followed by air cooling, exhibited higher bending strength values compared to those treated with recrystallization annealing. In the existing literature, there are no studies that address the influence of different post-processing routes, including machining, machining with conventional SP, machining with dual SP, and annealing followed by machining, on the flexural bending behavior of Ti6Al4V alloys produced by the SLM process. In the present study, three-point bending tests were conducted on five groups of specimens: as-built, milled, milled followed by traditional SP, milled followed by dual SP, and annealed before milling. To enable a detailed evaluation of the influence of post-processing treatments on static bending behavior, surface roughness measurements, microstructural characterizations, and post-fracture analyses were performed in addition to the three-point bending analyses. The findings were thoroughly analyzed to elucidate the underlying mechanisms governing the observed mechanical responses. By addressing a critical gap in the existing literature, this study provides a novel contribution to the field and advances the current understanding of how post-processing strategies affect the bending performance of components fabricated via SLM.

2 Experimental methodology

2.1 Specimen production

In this study, Ti6Al4V (Grade 5) powder produced by gas atomization was used. The powder particles exhibited a near-spherical morphology, which is favorable for flowability and uniform layer deposition during the SLM process. The particle size distribution analysis revealed that the powder particles' D10, D50, and D90 values were 18 µm, 31 µm, and 43 µm, respectively. The chemical composition of the powder presented in Table 1 complies with the ASTM B348/B348M-21 Standard [14]. All specimens were fabricated at a 45° angle to the production plate using the ENAVISION 250 SLM system, with the production parameters shown in Table 2. The SLM process was carried out under a controlled argon (Ar) atmosphere, and the O_2 content was maintained below 100 ppm. In production, 90° alternating scanning strategy was applied. For the bending test specimen, the length (l), width (w), and thickness (h) were determined as 60 × 10 × 6 mm, respectively, in accordance with the ASTM E290-22 standard [15]. In order to determine the relative density achieved by the applied processing parameters, three additional specimens with dimensions of 15 × 15 × 5 mm were fabricated.

Table 1 Chemical composition of Ti6Al4V powder (wt%)

C	O	*N*	H	Fe	Al	V	Other each	Other total	Ti
0.02	0.17	0.02	0.003	0.21	6.40	4.0	< 0.1	< 0.4	Balance

Table 2 SLM production parameters

Laser Power (W)	Scanning velocity (mm/s)	Hatch spacing (μm)	Layer thickness (μm)	Energy density (J/mm^3)
125	490	100	30	85

Table 3 Specimen names and explanations

Specimen name	Explanations
As-built	As-built
B	Milled
BS1	Milled + SP1
BS2	Milled + SP1 + SP2
BA	Annealed + milled

2.2 Post processes

As a result of the post-processes, specimens were classified into five groups. The specimen codes and descriptions are presented in Table 3.

2.2.1 Milling

Milling was performed on all specimens using the same parameters on a Haas VF4 CNC milling machine. The cutting parameters were set as follows: cutting speed (V_c) = 56.6 m/min, spindle speed (n) = 1125 rev/min, feed per tooth (f_z) = 0.045 mm/tooth, number of teeth (z) = 4, and axial depth of cut (a_p) = 0.2 mm. After milling all four surfaces, the dimensions of the specimens, which were originally produced as 60 × 12 × 8 mm (for all groups except the as-built), were reduced to 60 × 10 × 6 mm. Images of the specimens ready for the three-point bending test can be seen in Fig. 1.

2.2.2 Heat treatment

In order to examine the effects of heat treatment on the microstructure, surface roughness, and bending behaviour, specimens belonging to the BA group were subjected to heat treatment under a controlled Ar atmosphere. The details of the applied heat treatment are as follows: controlled heating from room temperature to 850 °C (average heating rate of 0.057 °C/s), holding at 850 °C for 2 h, and then furnace cooling from 850 °C to room temperature. This annealing process aimed to reduce residual stress and promote microstructural homogenization through phase transformation.

2.2.3 Shot peening

After milling, SP processes were performed on the BS1 and BS2 specimens using a Sigma SGM-1000P SP machine. While only conventional SP (SP1) was applied to the BS1 specimens, dual SP (SP1 + SP2) was applied to the BS2 specimens. The SP processes were applied to a single surface on the xy-plane, as shown in Fig. 2, in both specimen groups. The Almen intensity was set to 0.30 mm A Almen for both SP processes. In order to achieve this intensity, the required saturation time was determined in accordance with the ISO 26910-1:2023 standard [16] using an Electronics TSP-M Almen measuring device, an Almen strip holder, and A-type Almen strips. The saturation times were determined 139 s for SP1 and 122 s for SP2. The coverage of the SP process was set to 100% for each SP step. 52–55 HRC

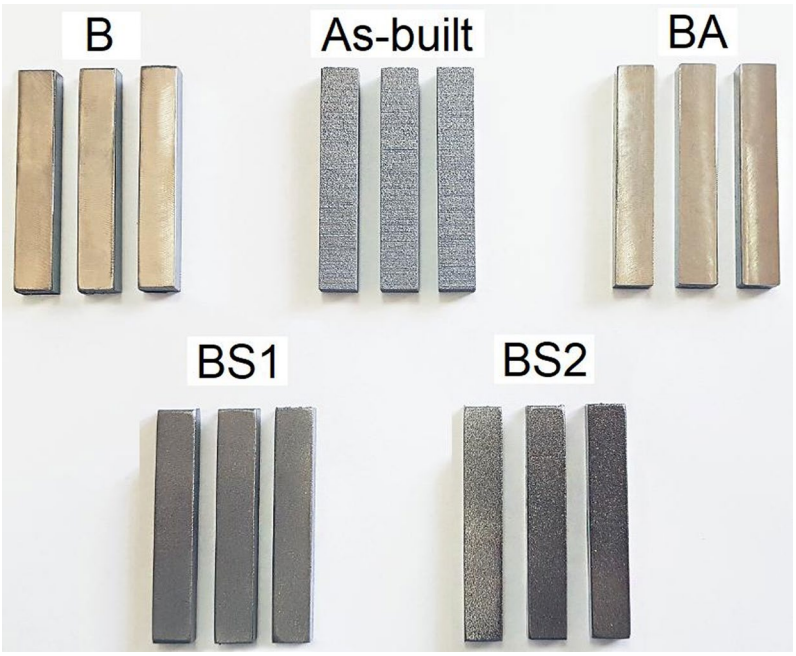


Fig. 1 The image of three-point bending specimens prepared for testing

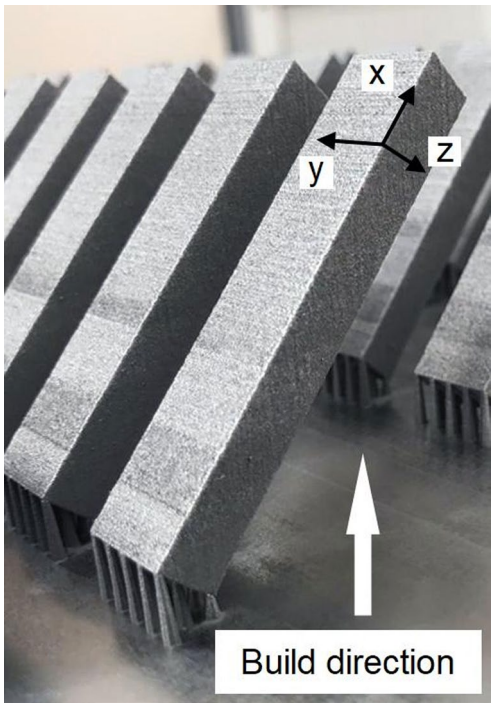


Fig. 2 Representation of the x, y, z axes and the build direction of the specimen

Table 4 Process parameters of the SP treatments

Specimen name	SP method	Almen intensity (mm A)	% 100 coverage time (s)	Diameter of balls (mm)
BS1	Conventional SP (SP1)	0.30	170	0.6
BS2	Dual SP (SP1 + SP2)	0.30 + 0.30	170 + 145	0.6 + 0.43

cast steel balls were used in both SP processes. The parameters of the SP processes performed are shown in Table 4.

2.3 Test procedures

The three-point bending tests were conducted using a Shimadzu AG-IS 100 kN machine at a 0.5 mm/min plunger displacement rate. The lower support rollers used in the test have a radius of 15 mm, while the plunger used for bending has a radius of 5 mm. In accordance with the ASTM E290-22 standard [15], the distance between the centers of the lower support rollers was set to 58 mm. The BS1 specimen positioned for the bending test is presented in the experimental setup shown in Fig. 3. As shown in Fig. 1, three specimens from each specimen group were subjected to testing, and the calculations were performed based on the average of the obtained results. Due to the specimens' rectangular

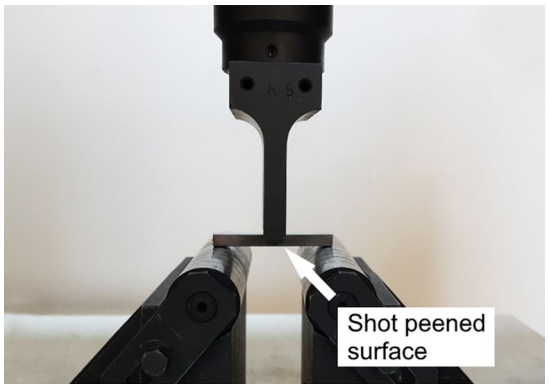


Fig. 3 The image of a BS1 specimen ready for the three-point bending test

cross-section, Eq. 1 [17] was used to calculate flexural stress (σ_f), and Eq. 2 [17] was used to calculate flexural strain (ε_f). Additionally, the (σ_f - ε_f) graph was created based on the results obtained.

$$\sigma_f = 3FL/2wh^2 \tag{1}$$

$$\epsilon_f = 6Dh/L^2 \tag{2}$$

Where F is the force applied at a given point (N), L is the distance between the centers of the lower supports (mm), w is the width of the specimen (mm), h is the thickness of the specimen (mm), and D is the maximum deflection of the specimen at the center (mm).

The surface roughness values were measured using a Mitutoyo SJ-410 roughness measurement device. In all specimens, measurements were performed in the x-axis direction, which is also the milling feed direction, as shown in Fig. 2. In each group, 10 measurements were taken using all three specimens, and the surface roughness values were obtained by averaging the results. In this study, R_a, R_z, R_c, R_{sk}, and R_{ku} parameters were measured to characterize surface roughness. However, due to its widespread use in the literature and its ability to represent the overall level of surface roughness, the R_a parameter, whose mathematical expression is given in Eq. (3) [18], was taken as the primary parameter for the comparative evaluation of surface roughness [19, 20]. The remaining roughness parameters were reported to provide complementary information on the geometric structure and height distribution characteristics of the surface profile. Brief descriptions of these parameters are provided in Table 5.

$$R_a = \frac{1}{l}\int_0^l |f(x)|\,dx \tag{3}$$

Table 5 Definitions of the surface roughness parameters (R_a, R_z, R_c, R_{sk}, R_{ku}) [18, 21, 22]

Parameter	Description
R_a	The arithmetic mean of the absolute values of the surface roughness profile ordinates.
R_z	The average value of the vertical distance between the highest peak and the deepest valley is determined over five consecutive sampling lengths.
R_c	Mean profile element height, obtained by averaging the vertical separations between the highest and lowest points of each profile element within the evaluation length.
R_{sk}	The skewness coefficient of the surface roughness profile reveals whether peaks or valleys dominate the surface morphology.
R_{ku}	The kurtosis of the surface roughness profile describes whether the surface height distribution is sharp-peaked or flat-topped compared to a normal distribution.

Where *f(x)* is the height of the peaks, *l* is the measuring length.

To investigate the microstructural changes induced by the applied heat treatment, metallographic examinations were conducted on one B and one BA specimen. Both specimens were analyzed in the same region located on the xy-plane. To examine the effects of the applied SP processes on the grain and phase structure, microstructural analyses were carried out on one BS2 specimen in the yz-plane, within a 50 µm depth interval under the SP-treated surface and another 50 µm depth interval above the non-SP-treated surface. The orientations of the xy and yz planes can be seen in Fig. 2. Prior to the examinations, the specimens underwent standard grinding and polishing procedures, followed by etching with Kroll's reagent (5 vol% nitric acid, 10 vol% hydrofluoric acid, and 85 vol% distilled water) for 20 to 45 s to reveal the microstructural features. Microstructural analyses of the B, BA, and BS2 specimens were carried out using a Nikon Eclipse LV150N optical microscope and a Zeiss Gemini SEM 500 scanning electron microscope (SEM). Following the three-point bending tests, fracture surface analyses of all specimens were conducted using a Nikon SMZ 745T stereo microscope and a Zeiss Gemini SEM 500.

The density measurements of the specimens were performed using a Micromeritics AccuPyc II 1340 helium pycnometer, which provides a volumetric measurement accuracy of ±0.03%. The relative density values were calculated by taking the bulk density of SLM-produced Ti6Al4V alloy as 4.43 g/cm³, based on the average of the results obtained from three specimens.

3 Results and discussion

3.1 Density measurements

The average density of the specimens was measured to be 4.41 g/cm³, while the relative density was calculated as 99.5%. These findings indicate that internal defects, including porosity and lack of fusion (LOF), are maintained within acceptable thresholds that the manufacturing quality is sufficient for the experimental procedures.

3.2 Surface roughness

The R_a surface roughness results of the specimens are presented in Fig. 4, while the R_z, R_c, R_{sk}, and R_{ku} results are provided in Table 6. The R_a value of the as-built specimen, which is not included in Fig. 4 in order to prevent scale domination, was measured as 17.05 µm.

When Table 6; Fig. 4 are evaluated together, it is observed that the applied machining, heat treatment, and SP processes have varying effects on the surface roughness characteristics. The high R_a value measured for the as-built specimen (17.05 µm) reflects the irregular, rough, and heterogeneous surface topography inherent to the SLM process [11]. A pronounced reduction in the R_a, R_z, and R_c values was observed for the B specimen after machining, suggesting that the irregular and sharp surface asperities characteristic of the SLM process were largely removed, resulting in a significant decrease in surface amplitude. The close similarity of the surface roughness parameters of the B and BA

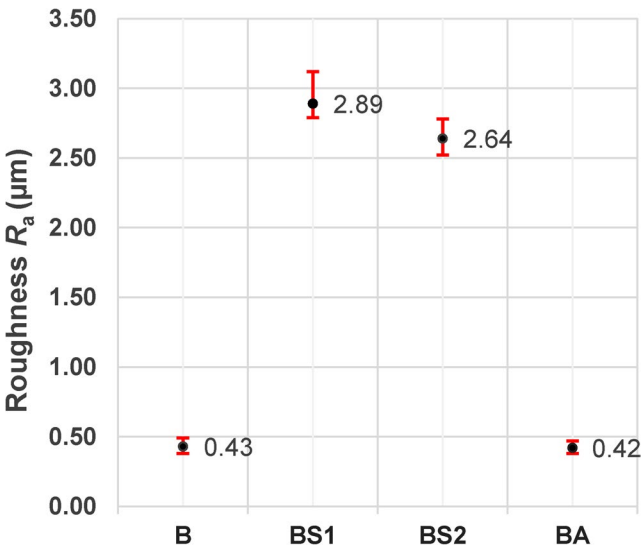


Fig. 4 R_a surface roughness results of the specimens

Table 6 R_z, R_c, R_{sk}, and R_{ku} surface roughness results of the specimens

Specimen	R_z (μm) [a]	R_c (μm) [a]	R_{sk} [b]	R_{ku} [b]
As-built	123.42	64.08	0.04 (−0.10; 0.17)	2.83 (2.66; 3.12)
B	2.73	1.75	−0.17 (−0.52; 0.26)	3.07 (2.35; 3.61)
BS1	18.60	11.35	−0.12 (−0.41; 0.20)	3.08 (2.54; 3.59)
BS2	17.02	10.11	0.27 (−0.15; 0.50)	2.97 (2.39; 3.42)
BA	2.61	1.67	−0.13 (−0.48; 0.30)	3.04 (2.47; 3.48)

[a] R_z and R_c are reported as average values to improve table readability.

[b] R_{sk} and R_{ku} are reported as average values with minimum and maximum values in parentheses (min; max) to reflect surface height distribution variability.

specimens indicates that the applied heat treatment did not lead to a noticeable change in surface roughness.

The SP1 treatment applied after machining resulted in a limited increase in the R_a, R_z, and R_c values of the BS1 specimen. This increase can be associated with the plastic deformation occurring on the surface during SP, as well as the formation of dimples and material pile-ups developing at the dimple edges [20, 23].

The R_{ku} value remaining below 3 in the as-built specimen indicates that the surface topography does not exhibit a statistically dominant sharp-peak character, which is characteristic of the SLM process [20]. In contrast, the increase of the R_{ku} value above 3 in the B and BA specimens subjected to machining, as well as in the BS1 specimen subjected to SP after machining, indicates that the height distribution becomes statistically more peaked despite the observed reduction in surface amplitude parameters (R_a, R_z, and R_c) [20]. This behavior can be associated with the micro-grooves and abrupt profile transitions formed during machining, which accentuate the tails of the height distribution through a relatively limited number of pronounced micro-peaks and micro-valleys [24, 25]. The more pronounced peaking tendency observed in the BS1 specimen can be explained by the dimple structures formed during the SP process and the material pile-ups (rims) developed at the edges of these structures, which contribute to the formation of additional sharp peaks on the surface [20, 23].

The SP2 treatment, applied at the same Almen intensity but using smaller-diameter shots (0.43 mm), resulted in a pronounced redistribution of the surface roughness parameters in the BS2 specimen. It was observed that the R_a, R_z, and R_c values of the BS2 specimen were lower than those of the BS1 specimen, which can be associated with the higher impact overlap (indentation overlap) provided by the smaller-diameter shots on the surface and their partial mitigation of the sharp surface asperities formed by the larger-diameter shots. These findings are consistent with the literature results reporting the surface roughness-reducing effect of using smaller-diameter shots in the SP process [11, 23]. On the other hand, the R_{ku} value of the BS2 specimen, being close to 3, may indicate that the surface height distribution is less influenced by extreme peaks and valleys, and tends toward a more Gaussian-like and homogeneous character. However, the Rsk value remaining in the positive range suggests that a slight predominance of peaks in the surface profile is still present. This observation may be associated with the denser and partially overlapping dimple structures produced by the smaller-diameter shots, together with microscale material pile-ups occurring at the dimple edges, which can contribute to the formation of numerous micro-peaks on the surface [11, 23].

The influence of surface roughness on bending behavior is primarily associated with the notch effect. A high level of surface roughness generates micro-notch-like features on the surface topography, which lead to local stress concentrations. Such conditions create an unfavorable environment for crack initiation and propagation in metals subjected to bending loads. In contrast, at relatively lower roughness levels, the notch effect is reduced, resulting in less pronounced stress concentrations and a delayed onset of cracking [26, 27]. The postponement of crack initiation allows for greater plastic deformation before bending failure, thereby contributing to an increase in ε_f. Moreover, due to the delayed occurrence of failure, σ_f is also enhanced [28–30]. Hence, minimizing surface roughness can be considered a critical factor in improving bending performance.

In their study, Fernandes et al. [28] observed a decrease in σ_f with increasing surface roughness in tungsten carbide–cobalt (WC-Co) hardmetals, which was attributed to stress concentration effects. In the study conducted by Lee et al. [29], it was also reported that high surface roughness values promoted premature fracture under bending deformation in rolled magnesium alloy AZ31. Consistent with these findings, Sneddon et al. [30] reported that in Ti6Al4V alloy specimens, a decrease in surface roughness values and the associated reduction in surface stress concentrations led to a significant increase in ε_f

3.3 Microstructure analyses

In the SLM process, melting occurs via laser within very short time intervals, resulting in extremely high thermal gradients (10^6 K/m). These high thermal gradients lead to extremely rapid cooling rates, reaching up to 10^8 K/s [5].

During the cooling stage of the SLM process of the Ti6Al4V alloy, extremely high cooling rates exceeding 410 °C/s lead to the formation of a high amount of metastable hexagonal α′ (SPH) phase within the β matrix [4, 6, 7]. In terms of the formed phases, the microstructure obtained in specimen B is consistent with the literature, as shown in Fig. 5a and b. The martensitic α′ laths observed in specimen B were located either within equiaxed prior β grains, as seen in Fig. 5a, or within columnar prior β grains, as shown in Fig. 5b. The martensitic α′ laths can be observed to extend parallel, perpendicular, or at a 45° angle to each other. The β transus temperature of the Ti6Al4V alloy is 980 ± 20 °C [31]. It is known that the α′ martensite phase in the microstructure of Ti6Al4V can transform into an α + β phase under the influence of the applied heat treatment parameters such as holding time, temperature, and cooling rate [32–35]. Following a heat treatment comprising a 2-hour holding at 850 °C, a temperature slightly below the β-transus of the Ti6Al4V alloy (980 ± 20 °C) and subsequent furnace cooling at an average rate of 0.022 °C/s, in the microstructure, the transformation to an α + β phase occurred. As seen in Fig. 5c, the α phase present in the microstructure of the BA specimen exhibits both lamellar and globular morphologies. In addition, grain boundary α can also be observed in Fig. 5c. Contrary to the appearance in Fig. 5c, the SEM image presented in Fig. 5d reveals the α phase as dark regions, whereas the β phase is observed with a brighter contrast. Previous studies have shown that the distribution and proportion of lamellar or globular α are related to all three parameters of the applied heat treatment: temperature, holding time, and cooling rate [34–36]. In the study conducted by Dabrowski [35], the effects of different cooling rates on the resulting microstructure were investigated, while keeping the heating temperature of the Ti6Al4V alloy at 1020 °C and the holding time at this temperature for 20 min constant. The microstructure obtained at a cooling rate of 0.015 °C/s was a mixture of lamellar and globular α phases, similar to the one received in the present study. In Dabrowski's study, at a cooling rate of 0.012 °C/s, the alpha phase was observed entirely in a globular morphology due to the relatively lower cooling rate [35].

There are studies in the literature reporting that the SP process results in grain/phase refinement on the material surface and at subsurface depths [4, 23, 32, 33]. In their study, Wang et al. [37] performed an SP process with 100% coverage on AISI 4340 steel; the grain size was measured to be approximately 2 µm at the surface of the SP-treated specimen, around 7 µm at a depth of 200 µm, and over 10 µm at a depth of 300 µm. In the study conducted by Kumar et al. [38], an SP process was performed on a Ti6Al4V alloy,

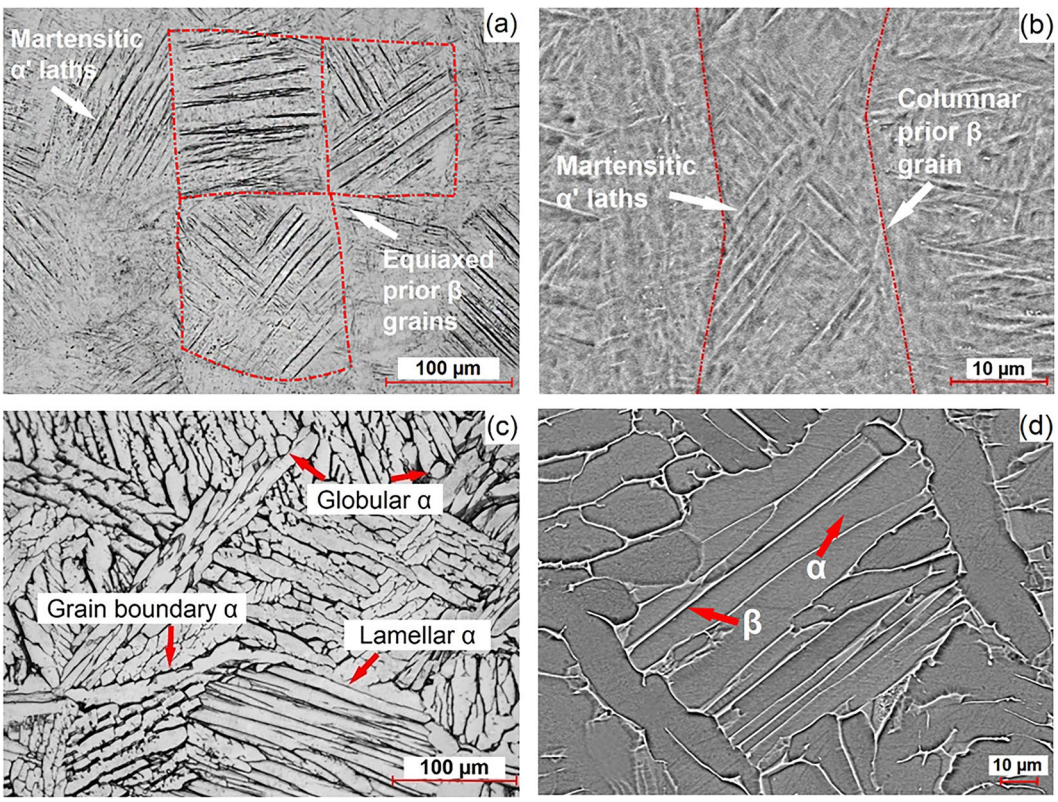


Fig. 5 Microstructure images obtained on the xy-plane: **a** equiaxed prior β grains observed in specimen B, **b** columnar prior β grain observed in specimen B, **c** grain boundary α phase and lamellar-globular α phases observed in specimen BA, **d** β and α phases observed in specimen BA

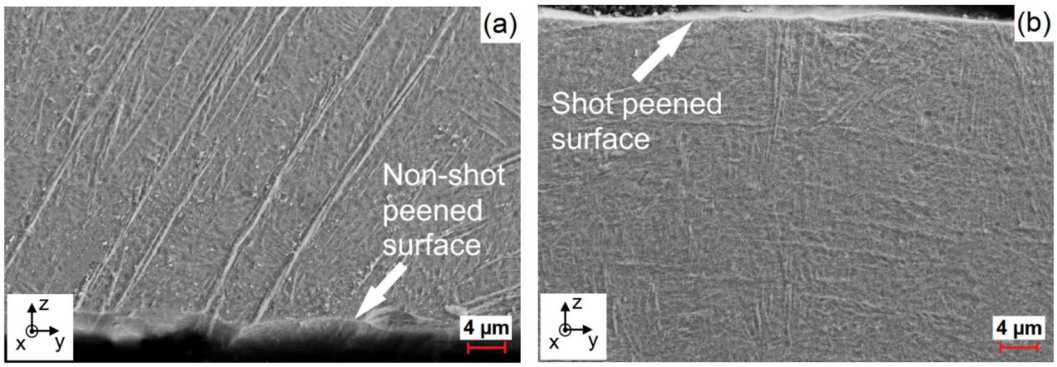


Fig. 6 The effect of the SP process performed on the BS2 specimen on the size of martensitic α′ laths: **a** image taken from a depth of 0–50 µm above the non-shot-peened surface, **b** image taken from a depth of 0–50 µm below the shot-peened surface

and it was reported that the process reduced the grain size to 16 ± 3 nm within the region extending up to a depth of 100 µm from the shot-peened surface. In this study, to determine the effect of the SP process on the microstructure, the SEM image taken from the 0–50 µm depth range above the non-shot-peened surface of the BS2 specimen is shown in Fig. 6a, while the SEM image obtained from the 0–50 µm depth range below the shot-peened surface is presented in Fig. 6b. It is observed that the SP process significantly reduced the size of the martensitic α′ laths.

3.4 Three-point bending analyses and fracture surface evaluation

The calculations carried out for each specimen group resulted in the obtained $\sigma_{f,\,max}$ values, which are seen in Fig. 7, whereas the σ_f - ε_f graph is seen in Fig. 8.

During the three-point bending test, a stress distribution occurs in the specimens as illustrated in Fig. 9, where the tensile stresses reach their maximum values at the bottom surface of the specimen mounted in the test setup. Under the influence of this condition, the bottom surface becomes the most critical area for crack initiation and propagation [39]. It is known that, under the influence of the extremely high thermal gradients generated during the SLM process and the associated shrinkage tendency occurring during the cooling stage, tensile residual stresses form at the surface and near-surface regions of the SLMed Ti6Al4V specimens [40–43]. Previous studies, based on both experimental and numerical investigations, have shown that machining is effective in inducing compressive residual stresses at depths of 0–100 µm within specimens [44–46]. When the $\sigma_{f,\,max}$ values of the B and as-built specimens are compared, the 23% increase observed in the B specimen can be attributed to the combined influence of three factors. First, the dramatic reduction in surface roughness after machining, from an average R_a of 17.05 µm in the as-built specimen to 0.43 µm in the B specimen, mitigates stress concentrations on the surface profile, thereby delaying crack initiation and facilitating the attainment of higher σ_f values. Second, the necessity of overcoming the compressive residual stresses present in the surface and subsurface regions prior to bending further contributes to the increase in $\sigma_{f,\,max}$. Finally, machining-induced cold plastic deformation leads to an increase in dislocation density. Since the deformation conditions during milling did not reach the recrystallization temperature, this increase in dislocation density also plays a role in enhancing $\sigma_{f,\,max}$. Together, these mechanisms account for the improved $\sigma_{f,\,max}$ value of the machined specimens [28, 29, 47–49]. The higher ε_f value achieved by the B specimen compared to the as-built specimen is associated with the dramatic reduction in surface roughness amplitude parameters (R_a, R_z, and R_c) resulting from the milling. It is considered that the reduction in surface roughness decreased the notch effect, thereby delaying crack initiation and propagation, and consequently allowing for greater plastic deformation before bending failure [30, 50].

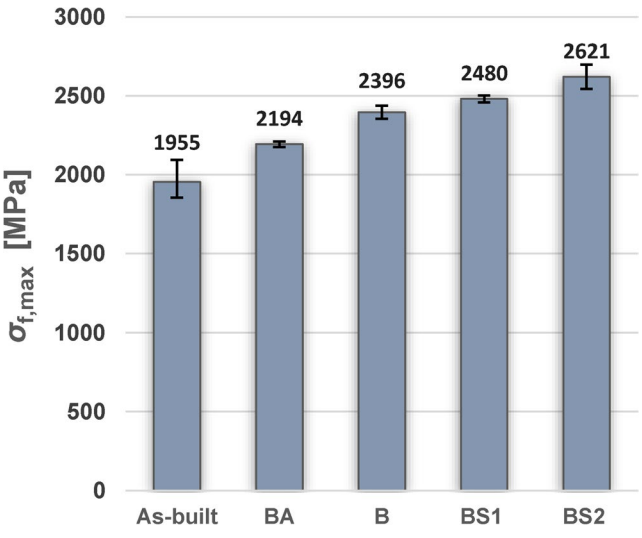


Fig. 7 $\sigma_{f,\,max}$ values of the specimens

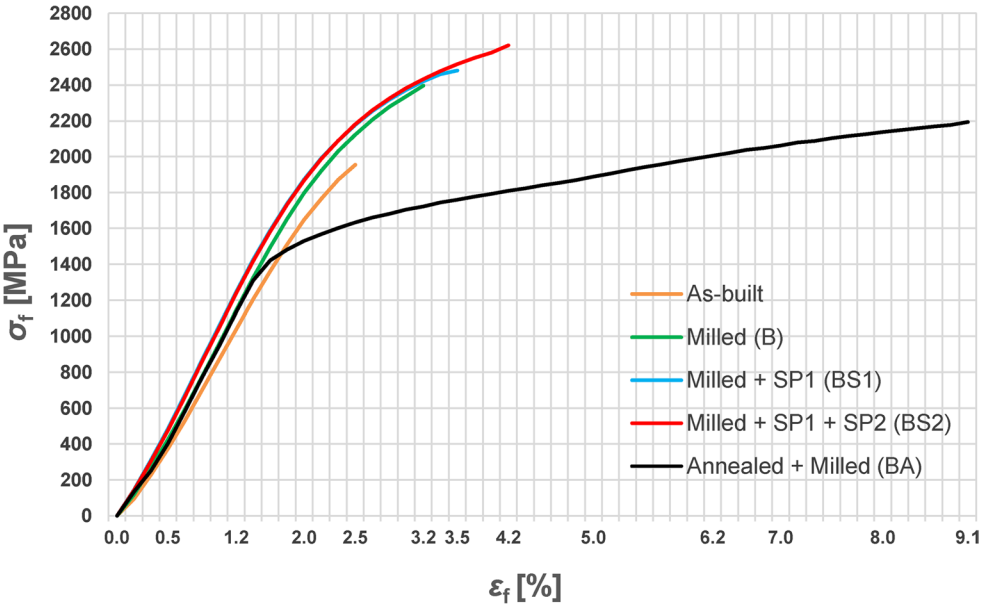


Fig. 8 σ_f-ε_f graph of the specimens

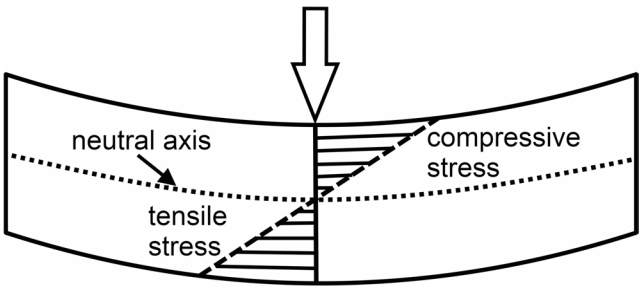


Fig. 9 The distribution of stresses generated during bending [39]

It is known that the SP process is highly effective in generating compressive residual stresses on the treated surface and in subsurface regions, and that it also increases dislocation density at effective depths due to the cold plastic deformation induced on the surface [11, 51, 52]. The fact that the $\sigma_{f,\,max}$ value obtained for the BS1 specimen is higher than that for the B specimen, and that the $\sigma_{f,\,max}$ value obtained for the BS2 specimen is higher than that for the BS1 specimen, is considered to be associated with the combined effect of higher compressive residual stresses, higher dislocation density and finer martensitic α′ laths induced by the SP1 and SP1 + SP2 processes [51–54]. In the study conducted by İrizalp and Saklakoğlu [55], tensile and microstructural analyses were performed on two groups of specimens, one subjected to LSP and the other untreated. It was reported that the LSP process caused significant grain refinement in the specimens and that, based on the tensile test results, the grain refinement led to notable increases in both tensile strength and elongation. The marked improvement in ductility observed in the LSP-treated specimens was attributed to the grain refinement. Furthermore, it was stated that the applied LSP process contributed to the formation of a nanostructured material, resulted in a reduction in stacking fault energy, increased the presence of stacking faults and twinning within the microstructure, and thereby enhanced the dislocation storage capacity, positively contributing to the improvement in ductility. It is observed that the ε_f values obtained for the BS1 and BS2 specimens are slightly higher than those obtained for the B specimen. This difference is considered to be associated with the reduction in the size of the martensitic α′ phase observed in Fig. 6, which occurred in the BS1 and BS2 specimens under the effect of SP, similar to the findings reported in the study by İrizalp and Saklakoğlu [55]. In addition to the mechanisms discussed above, when compared with the R_{ku} values obtained for the B and BS1 specimens, it is observed that the R_{ku} value of the BS2 specimen decreases to 2.97, indicating a more Gaussian-like height distribution. This reduction in R_{ku} is considered to limit local stress concentrations by reducing the sharpness of surface peaks and valleys, and to exhibit an effect that is consistent with a delay in crack initiation and propagation. This condition is thought to have provided an additional contribution, from a surface integrity perspective, to the increases observed in both $\sigma_{f,\,max}$ and ε_f values for the BS2 specimen [56, 57].

The $\sigma_{f,\,max}$ value obtained for the BA specimen, which was machined after annealing, was 12% higher than that of the as-built specimen, although it remained below that of the other groups. This enhancement is attributed to the pronounced delay in crack initiation, resulting from the combined effects of the increased ductility induced by the microstructural transformation during annealing and the substantial reduction in surface roughness amplitude parameters achieved through machining [30, 50]. The lower $\sigma_{f,\,max}$ value observed in the BA specimen compared to the B

specimen is considered to be associated with the relatively higher total amount of dislocations in the B specimen, which results from both the manufacturing process and the milling operation. In contrast, the BA specimen was subjected to milling under the same parameters after annealing, and this is considered to have resulted in a comparatively lower dislocation density. Furthermore, the α + β phase transformation that occurred in the microstructure of the BA specimen as a result of annealing is also thought to contribute to this outcome. Compared to the much finer martensitic α′ laths, the coarser α phase provides a more conducive environment for dislocation movement due to its larger structure [35, 48, 49]. In this study, the effect of phase size observed in the B and BA specimens on bending strength shows similarity with the findings reported by Yeşilkaya et al. [13], who examined the influence of phase size on bending strength under different heat treatment conditions. In their study, specimens subjected to heat treatment at 790 °C for 1 h, followed by air cooling, exhibited a microstructure containing martensitic α′ phase, whereas the microstructure of the specimens subjected to recrystallization annealing contained lamellar α phase. It was reported that, in relation to these microstructures, the specimens exposed to recrystallization annealing exhibited lower bending strength values. When the ε_f value obtained for the BA specimen is examined, a dramatic increase of 264% is observed compared to the as-built specimen, and about 184% compared to the B specimen. The primary reason for this outcome is the α + β phase transformation that occurred in the microstructure as a result of heat treatment, while the low surface roughness level (R_a: 0.42 µm), particularly in comparison with the as-built specimen, appears as a secondary factor supporting this result [2, 13, 58].

Macro images obtained after the three-point bending test for one specimen from each group are presented in Fig. 10.

When the macro images are examined, it is observed that the cracks in the as-built and B specimens propagated across the entire cross-section, resulting in complete fracture. Similarly, a complete fracture also occurred in the BS1 and BS2 specimens, and the general character of the crack path does not exhibit a pronounced difference compared to the as-built and B specimens. This indicates that, at the macro scale, the crack propagation behavior offers limited distinction among the specimens, except for the BA specimen. In the BA specimen, examination of Fig. 9e and e' reveal crack initiation and limited crack propagation; however, it is evident that the crack did not traverse the entire cross-section. Further examination of Fig. 9e" shows that no distinct crack formed on the right-side surface of the specimen, indicating that complete fracture did not occur in the BA specimen and that it exhibited a fracture profile different from those of the other specimen groups. This observation suggests delayed crack propagation and enhanced ductility in the BA specimen. Following the heat treatment applied to the BA specimen, the complete dissolution of the martensitic α′ phase and the consequent transformation into a stable α + β microstructure significantly improved the material's ductility. The coarser morphology of the α phase provides a more favorable pathway for dislocation motion, thereby contributing to an increased plastic deformation capacity of the material [11].

Although the crack initiation point cannot be directly identified from the macro images, it is well known that, under the loading configuration applied in a three-point bending test, the surfaces where tensile stresses reach their maximum values constitute the most critical regions for crack initiation. Considering the test setup used in this study, the upper surfaces visible in the left-side and right-side views in Fig. 10 represent the most critical regions for crack initiation, and these surfaces correspond to the bottom surfaces shown in Fig. 9. Therefore, it is mechanically expected that crack initiation occurred from these surfaces [39].

The SEM fracture surface images are presented in Fig. 11, with a particular focus on manufacturing-induced defect regions located along the crack propagation path, which have a significant influence on the crack orientation.

The defects observed in the SEM fractography images primarily consist of LOF–type defects and porosities. In the SLM process, LOF defects arise as a result of insufficient melting between adjacent melt pools or successive layers; this condition is generally associated with process-related parameters such as insufficient energy input, inappropriate scanning strategies, local powder bed irregularities, and local disturbances in heat accumulation [8, 11]. LOF-type defects develop in the form of irregularly shaped voids with sharp corners and often contain unmelted or partially sintered powder particles; due to these morphological characteristics, they cause pronounced local stress concentrations under mechanical loading [2, 9]. In contrast, the porosities observed on the fracture surfaces are mainly formed as a result of gases trapped within the initial powder or gases generated during melting that cannot be released during solidification. These porosities generally exhibit a more spherical or rounded morphology and therefore present a more geometrically regular structure compared to LOF defects [9, 10].

Examination of the fracture surfaces suggests that these defects are predominantly distributed in an irregular manner and, owing to their sharp geometries, give rise to local stress concentrations, thereby playing a dominant role in the formation of crack initiation sites and, in particular, in determining the crack propagation path. Indeed, it has been widely reported in the literature that, particularly due to

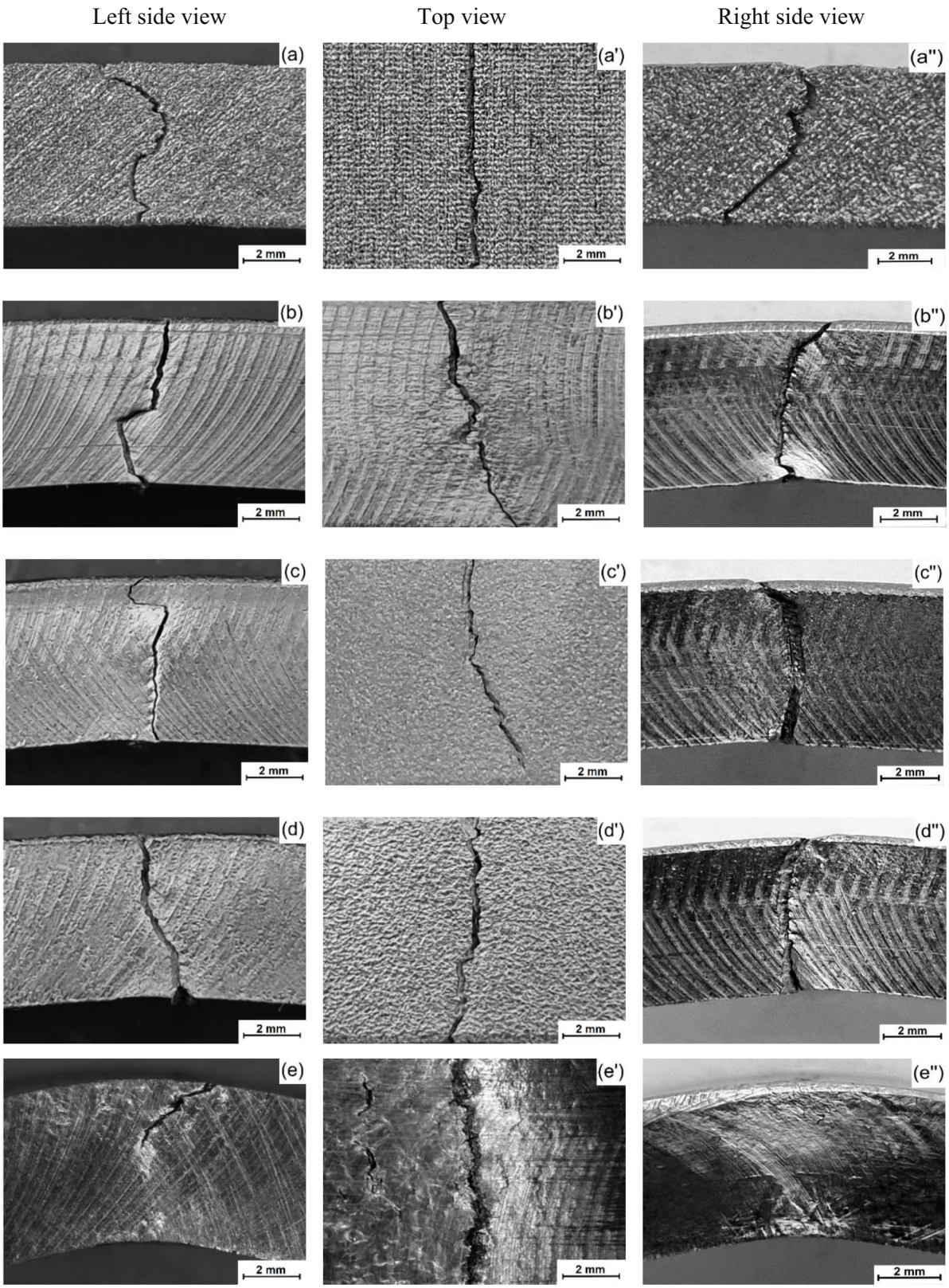


Fig. 10 Post-fracture macro images of specimens **a**, **a**', **a**": as-built, **b**, **b**', **b**": specimen B, **c**, **c**', **c**": specimen BS1, **d**, **d**', **d**": specimen BS2, **e**, **e**', **e**": specimen BA

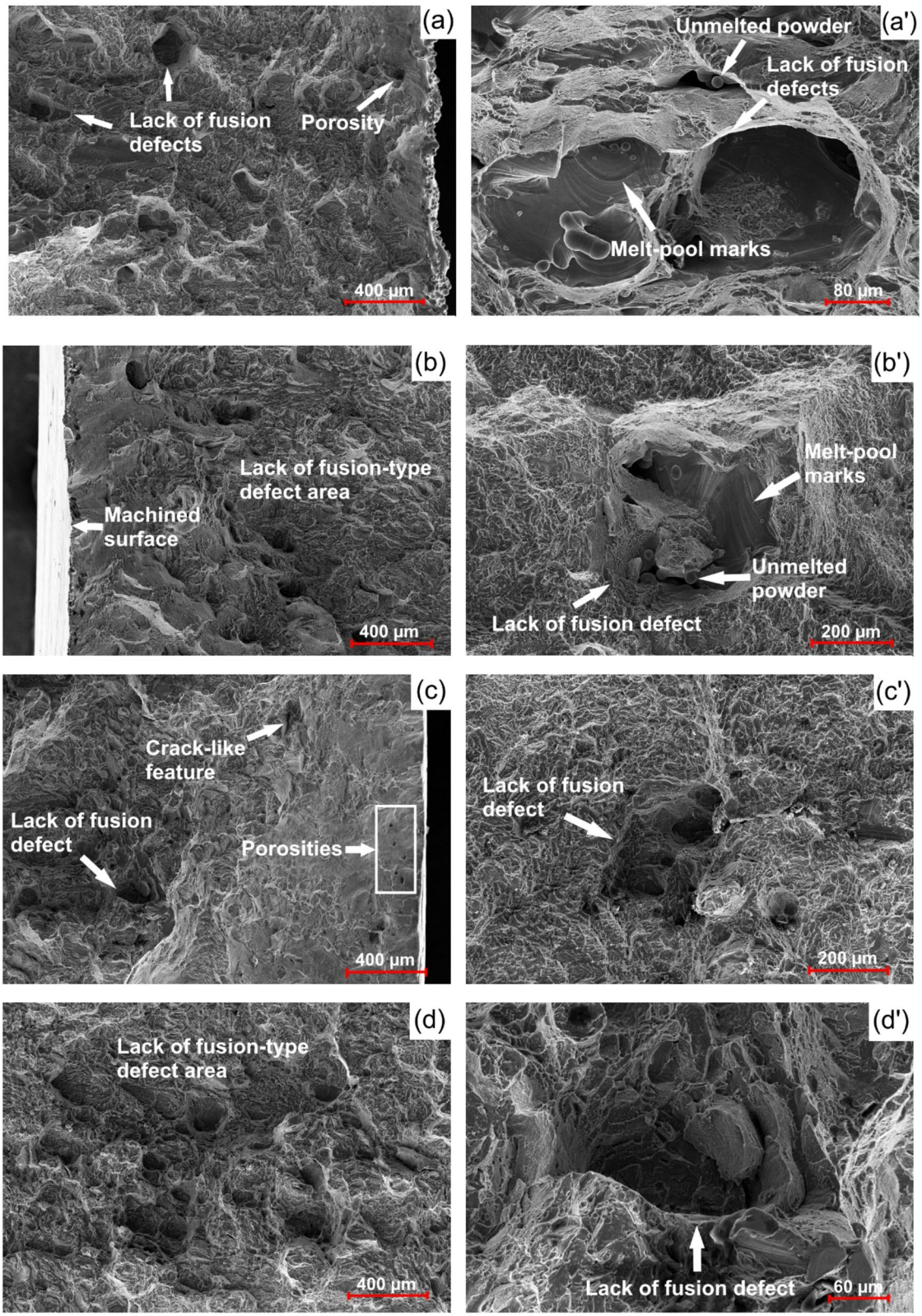


Fig. 11 Representative SEM fractography images highlighting manufacturing-induced defects along the crack propagation paths on the fracture surfaces of specimens fractured under three-point bending **a**, **a**': as-built, **b**, **b**': specimen B, **c**, **c**': specimen BS1, **d**, **d**': specimen BS2

their irregular shapes, unbonded surfaces, and sharp edges, LOF-type defects create an effective notch effect, which facilitates crack initiation and largely directs crack propagation along the defect geometry [2, 7]. In contrast, owing to their more rounded morphologies, porosities generally generate relatively lower stress concentrations; however, it is known that they can still contribute to crack propagation when present at appropriate sizes and locations [9, 10]. Considering that, under three-point bending, the maximum tensile stresses are concentrated at the surface and in the near-surface regions, the tendency of a surface-initiated crack to exhibit a preferential orientation along regions containing manufacturing-induced defects as it propagates within the material is considered a mechanically expected behavior and is consistent with the literature [28, 29, 39].

Dimple-like morphological features locally observed around LOF defects indicate that limited and localized plastic deformation occurred during fracture. However, a combined evaluation of the σ_f–ε_f curves and the fracture surface images shows that the fracture behavior of the as-built, B, BS1, and BS2 specimens was governed predominantly by a defect-controlled and essentially brittle character rather than by a ductile fracture mechanism.

4 Conclusions

This study investigated in detail the effects of machining, conventional and dual SP applied after machining, and heat treatment followed by machining on the bending behavior of SLM-produced Ti6Al4V alloy.

Machining reduced Ra from 17.05 µm (as-built) to 0.43 µm in the machined specimen (B), which markedly lowered the notch effect and delayed crack initiation. This reduction in surface roughness played a decisive role in the increases observed in both σf, max and εf when the B specimen was compared with the as-built specimen. While conventional SP caused a slight increase in roughness, the secondary SP with smaller-diameter balls decreased surface roughness amplitude again, demonstrating that decreasing surface roughness through dual SP can be achieved without compromising mechanical integrity. In addition to reducing surface amplitude parameters, dual SP also promoted a more homogeneous surface height distribution, as indicated by the Rku values approaching 3, suggesting a surface profile closer to a Gaussian-like character.

Machining alone improved $\sigma_{f,\,max}$ by 23% due to reduced surface roughness, induced compressive residual stresses, and increased dislocation density. Dual SP elevated $\sigma_{f,\,max}$ by 34% compared to the as-built condition, highlighting the synergistic role of compressive stress induction, martensitic α′ lath refinement, the reduction in surface roughness, and the increased dislocation density generated by machining combined with SP1 and SP2. This indicates that SP treatments can provide additional strengthening beyond machining alone.

Fracture surface analyses revealed that, in the as-built, B, BS1 (machined and conventionally shot-peened), and BS2 (machined and dual shot-peened) specimens, the crack propagation path was governed primarily by intrinsic defects specific to the SLM process. Under bending loading, a predominantly quasi-brittle fracture character was observed in all specimens except the annealed and machined (BA) specimen. Macro-scale fracture observations showed that, unlike the other specimen groups, the BA did not undergo complete fracture, exhibiting only crack initiation and limited crack propagation. The BA specimen exhibited a 264% increase in ε_f relative to the as-built condition and a 184% increase compared to the B specimen. This behavior is attributed to the α + β transformation during annealing and improved surface quality, which effectively delayed crack growth and promoted a more ductile bending response in SLMed Ti6Al4V. In addition, when the BA is compared with the as-built specimen, it is evident that the reduction in surface roughness provided a secondary yet still effective contribution by delaying crack initiation, thereby supporting the increases observed in both $\sigma_{f,\,max}$ and ε_f. Overall, these results indicate that the combined influence of phase morphology and surface quality can shift the fracture response from a brittle-dominated to a more ductile character under bending in SLMed Ti6Al4V.

In the existing literature, there are no studies that address the effects of different post-processing routes, including machining, machining followed by conventional SP, machining followed by dual SP, and annealing followed by machining, on the static bending behavior of SLMed Ti6Al4V alloys. By integrating multiscale characterization with bending tests, this study demonstrates that these routes can contribute to the improvement of bending behavior, thus providing valuable insights and constituting a unique contribution to the field.

Acknowledgements The authors would like to thank Celal Bayar University (Project code: 2020−121) and Ermaksan Makina Sanayi ve Ticaret A.Ş. for providing financial support.

Author contributions Sinan ÖNDER: Conceptualization, Methodology, Validation, Formal analysis, Investigation, Data Curation, Writing – Original Draft, Writing – Review & Editing, Visualization. Nurşen SAKLAKOĞLU: Conceptualization, Validation, Resources, Writing – Review & Editing, Supervision, Project administration, Funding acquisition. Ahmet SEVER: Software, Investigation, Resources, Funding acquisition.Gökhan BAŞAR: Investigation, Writing – Original Draft.

Funding Open access funding provided by the Scientific and Technological Research Council of Türkiye (TÜBİTAK). This study was financially supported by Celal Bayar University (Project code: 2020−121) and Ermaksan Makina Sanayi ve Ticaret A.Ş.

Declarations

Competing interests The authors declare that they have no known competing financial interests or personal relationships that could have appeared to influence the work reported in this paper.

Open Access This article is licensed under a Creative Commons Attribution 4.0 International License, which permits use, sharing, adaptation, distribution and reproduction in any medium or format, as long as you give appropriate credit to the original author(s) and the source, provide a link to the Creative Commons licence, and indicate if changes were made. The images or other third party material in this article are included in the article's Creative Commons licence, unless indicated otherwise in a credit line to the material. If material is not included in the article's Creative Commons licence and your intended use is not permitted by statutory regulation or exceeds the permitted use, you will need to obtain permission directly from the copyright holder. To view a copy of this licence, visit http://creativecommons.org/licenses/by/4.0/.

References

1. Baufeld B, Brandl E, van der Biest O (2011) Wire based additive layer manufacturing: comparison of microstructure and mechanical properties of Ti–6Al–4V components fabricated by laser-beam deposition and shaped metal deposition. J Mater Process Technol 211:1146–1158. https://doi.org/10.1016/j.jmatprotec.2011.01.018
2. Leuders S, Lieneke T, Lammers S et al (2014) On the fatigue properties of metals manufactured by selective laser melting – The role of ductility. J Mater Res 29:1911–1919. https://doi.org/10.1557/jmr.2014.157
3. Cui C, Hu B, Zhao L, Liu S (2011) Titanium alloy production technology, market prospects and industry development. Mater Des 32:1684–1691. https://doi.org/10.1016/j.matdes.2010.09.011
4. Lütjering G, Williams JC (2003) Titanium. Engineering materials and processes. Springer, Berlin, Heidelberg. https://doi.org/10.1007/978-3-540-73036-1
5. Yang J, Yu H, Yin J et al (2016) Formation and control of martensite in Ti-6Al-4V alloy produced by selective laser melting. Mater Des 108:308–318. https://doi.org/10.1016/j.matdes.2016.06.117
6. Ahmed T, Rack HJ (1998) Phase transformations during cooling in α+β titanium alloys. Mater Sci Eng A 243:206–211. https://doi.org/10.1016/S0921-5093(97)00802-2
7. Simonelli M, Tse YY, Tuck C (2014) Effect of the build orientation on the mechanical properties and fracture modes of SLM Ti–6Al–4V. Mater Sci Eng A 616:1–11. https://doi.org/10.1016/j.msea.2014.07.086
8. Rafi HK, Karthik NV, Gong H et al (2013) Microstructures and mechanical properties of Ti6Al4V parts fabricated by selective laser melting and electron beam melting. J Mater Eng Perform 22:3872–3883. https://doi.org/10.1007/s11665-013-0658-0
9. Leuders S, Thöne M, Riemer A et al (2013) On the mechanical behaviour of titanium alloy TiAl6V4 manufactured by selective laser melting: fatigue resistance and crack growth performance. Int J Fatigue 48:300–307. https://doi.org/10.1016/j.ijfatigue.2012.11.011
10. Qiu C, Adkins NJE, Attallah MM (2013) Microstructure and tensile properties of selectively laser-melted and of hiped laser-melted Ti–6Al–4V. Mater Sci Eng A 578:230–239. https://doi.org/10.1016/j.msea.2013.04.099
11. Önder S, Saklakoğlu N, Sever A (2023) Selective laser melting of Ti6Al4V alloy: effect of post-processing on fatigue life, residual stress, microstructure, microhardness and surface roughness. Mater Charact 196:112571. https://doi.org/10.1016/j.matchar.2022.112571
12. Wu MW, Lai PH (2016) The positive effect of hot isostatic pressing on improving the anisotropies of bending and impact properties in selective laser melted Ti-6Al-4V alloy. Mater Sci Eng A 658:429–438. https://doi.org/10.1016/j.msea.2016.02.023
13. Yesilkaya KK, Usta Y, Aycan MF, Demir T (2022) Experimental and numerical investigation on bending behavior of Ti-6Al-4V parts produced by additive metal laser sintering. J Mater Eng Perform 31:286–296. https://doi.org/10.1007/s11665-021-06192-3
14. ASTM B348/B348M-21 Standard Specification for Titanium and Titanium Alloy Bars and Billets (2021) https://doi.org/10.1520/B0348_B0348M-21
15. ASTM E290-22 (2022) Test methods for bend testing of material for ductility https://doi.org/10.1520/E0290-22
16. ISO 26910-1:2023 Springs - shot peening part 1: General procedures (2023)
17. Callister WD, Rethwisch DG (2018) Materials science and engineering: an introduction, 10th edn. Wiley, Hoboken
18. ISO 21920-2:2021 Geometrical product specifications (GPS) - Surface texture: Profile Part 2: Terms, definitions and surface texture parameters (2021)
19. Schmähling J, Hamprecht FA, Hoffmann DMP (2006) A three-dimensional measure of surface roughness based on mathematical morphology. Int J Mach Tools Manuf 46:1764–1769. https://doi.org/10.1016/j.ijmachtools.2005.12.003
20. Bagherifard S, Ghelichi R, Guagliano M (2012) Numerical and experimental analysis of surface roughness generated by shot peening. Appl Surf Sci 258:6831–6840. https://doi.org/10.1016/j.apsusc.2012.03.111
21. JIS B 0601 Geometrical product specification (GPS) – surface texture: Profile method – terms, definitions and surface texture parameters (2001)
22. JIS B 0031 (2003) Geometrical product specifications (GPS) – indication of surface texture in technical product Documentation
23. Ghanbari S, Bahr DF (2020) Predictions of decreased surface roughness after shot peening using controlled media dimensions. J Mater Sci Technol 58:120–129. https://doi.org/10.1016/j.jmst.2020.03.075
24. Pawlus P, Reizer R, Wieczorowski M (2022) Parametric characterization of machined textured surfaces. Mater (Basel) 16:163. https://doi.org/10.3390/ma16010163
25. Whitehouse DJ (2010) Handbook of surface and nanometrology, 2nd edn. CRC, Boca Raton
26. Murakami Y (2019) Metal fatigue: effects of small defects and nonmetallic inclusions, 2nd edn. Academic, Amsterdam
27. Pluvinage G, Gjonaj M (2001) Notch effects in fatigue and fracture. Springer, Dordrecht
28. Fernandes JJ, Da Silva CP, Rosa LG, Martins CS (1994) Effects of surface roughness on the flexural strength of a hardmetal. J Mater Sci 29:2008–2012. https://doi.org/10.1007/BF01154674
29. Lee GM, Lee JU, Park SH (2023) Effects of surface roughness on bending properties of rolled AZ31 alloy. J Magnes Alloy 11:1224–1235. https://doi.org/10.1016/j.jma.2021.11.029
30. Sneddon S, Xu Y, Dixon M et al (2021) Sensitivity of material failure to surface roughness: A study on titanium alloys Ti64 and Ti407. Mater Des 200:109438. https://doi.org/10.1016/j.matdes.2020.109438
31. Momeni A, Abbasi SM (2010) Effect of hot working on flow behavior of Ti–6Al–4V alloy in single phase and two phase regions. Mater Des 31:3599–3604. https://doi.org/10.1016/j.matdes.2010.01.060

32. Li H, Jia D, Yang Z et al (2021) Effect of heat treatment on microstructure evolution and mechanical properties of selective laser melted Ti–6Al–4V and TiB/Ti–6Al–4V composite: A comparative study. Mater Sci Eng A 801:140415. https://doi.org/10.1016/j.msea.2020.140415
33. Yan X, Yin S, Chen C et al (2018) Effect of heat treatment on the phase transformation and mechanical properties of Ti6Al4V fabricated by selective laser melting. J Alloys Compd 764:1056–1071. https://doi.org/10.1016/j.jallcom.2018.06.076
34. Vrancken B, Thijs L, Kruth J-P, Van Humbeeck J (2012) Heat treatment of Ti6Al4V produced by selective laser melting: microstructure and mechanical properties. J Alloys Compd 541:177–185. https://doi.org/10.1016/j.jallcom.2012.07.022
35. Dąbrowski R (2011) The kinetics of phase transformations during continuous cooling of the Ti6Al4V alloy from the single-phase β range. Arch Metall Mater 56:703–707. https://doi.org/10.2478/v10172-011-0077-x
36. Stefansson N, Semiatin SL, Eylon D (2002) The kinetics of static globularization of Ti-6Al-4V. Metall Mater Trans A 33:3527–3534. https://doi.org/10.1007/s11661-002-0340-x
37. Wang C, Wang L, Wang X, Xu Y (2018) Numerical study of grain refinement induced by severe shot peening. Int J Mech Sci 146–147:280–294. https://doi.org/10.1016/j.ijmecsci.2018.08.005
38. Kumar S, Chattopadhyay K, Singh SR, Singh V (2017) Surface nanostructuring of Ti-6Al-4V alloy through ultrasonic shot peening. Int J Surf Sci Eng 11:23. https://doi.org/10.1504/IJSURFSE.2017.082949
39. Kuhn H, Medlin D (2000) Mechanical testing and Evaluation. ASM handbook, vol 8. ASM International, Materials Park
40. Mishurova T, Cabeza S, Artzt K et al (2017) An assessment of subsurface residual stress analysis in SLM Ti-6Al-4V. Materials 10:348. https://doi.org/10.3390/ma10040348
41. Yakout M, Elbestawi MA, Veldhuis SC (2020) A study of the relationship between thermal expansion and residual stresses in selective laser melting of Ti-6Al-4V. J Manuf Process 52:181–192. https://doi.org/10.1016/j.jmapro.2020.01.039
42. Xiao Z, Chen C, Zhu H et al (2020) Study of residual stress in selective laser melting of Ti6Al4V. Mater Des 193:108846. https://doi.org/10.1016/j.matdes.2020.108846
43. Xiao Z, Chen C, Hu Z et al (2020) Effect of rescanning cycles on the characteristics of selective laser melting of Ti6Al4V. Opt Laser Technol 122:105890. https://doi.org/10.1016/j.optlastec.2019.105890
44. Javidi A, Rieger U, Eichlseder W (2008) The effect of machining on the surface integrity and fatigue life. Int J Fatigue 30:2050–2055. https://doi.org/10.1016/j.ijfatigue.2008.01.005
45. Masoudi S, Amini S, Saeidi E, Eslami-Chalander H (2015) Effect of machining-induced residual stress on the distortion of thin-walled parts. Int J Adv Manuf Technol 76:597–608. https://doi.org/10.1007/s00170-014-6281-x
46. Weber D, Kirsch B, Chighizola CR et al (2021) Analysis of machining-induced residual stresses of milled aluminum workpieces, their repeatability, and their resulting distortion. Int J Adv Manuf Technol 115:1089–1110. https://doi.org/10.1007/s00170-021-07171-7
47. Li B, Zhang S, Hu R, Zhang X (2020) Dislocation density and grain size evolution in hard machining of H13 steel: numerical and experimental investigation. J Mater Res Technol 9:4241–4254. https://doi.org/10.1016/j.jmrt.2020.02.051
48. Ding L, Zhang X, Richard Liu C (2014) Dislocation density and grain size evolution in the machining of Al6061-T6 alloys. J Manuf Sci Eng 136:041020. https://doi.org/10.1115/1.4027675
49. Hasebe T (2023) Dislocation theory and metallurgy. In: Voyiadjis GZ (ed) Field theory of multiscale plasticity. Cambridge University Press, Cambridge, pp 3–85. https://doi.org/10.1017/9781108874069.003
50. Pilkey WD, Pilkey DF (2007) Peterson's stress concentration factors, 3rd edn. Wiley, Hoboken, NJ
51. Wang C, Lai Y, Wang L, Wang C (2020) Dislocation-based study on the influences of shot peening on fatigue resistance. Surf Coat Technol 383:125247. https://doi.org/10.1016/j.surfcoat.2019.125247
52. Lin Q, Liu H, Zhu C et al (2020) Effects of different shot peening parameters on residual stress, surface roughness and cell size. Surf Coat Technol 398:126054. https://doi.org/10.1016/j.surfcoat.2020.126054
53. Hall EO (1951) The deformation and ageing of mild steel: III discussion of results. Proc Phys Soc Sect B 64:747–753. https://doi.org/10.1088/0370-1301/64/9/303
54. Petch NJ (1953) The cleavage strength of polycrystals. J Iron Steel Inst 174:25–28
55. Gencalp Irizalp S, Saklakoglu N (2016) High strength and high ductility behavior of 6061-T6 alloy after laser shock processing. Opt Lasers Eng 77:183–190. https://doi.org/10.1016/j.optlaseng.2015.08.004
56. Lee S, Rasoolian B, Silva DF et al (2021) Surface roughness parameter and modeling for fatigue behavior of additive manufactured parts: A non-destructive data-driven approach. Addit Manuf 46:102094. https://doi.org/10.1016/j.addma.2021.102094
57. Hebert J, Khonsari MM (2024) Effect of surface roughness and Polishing orientation on fatigue life and fracture fatigue entropy. Fatigue Fract Eng Mater Struct 47:1514–1530. https://doi.org/10.1111/ffe.14260
58. Ter Haar GM, Becker TH (2018) Selective laser melting produced Ti-6Al-4V: Post-process heat treatments to achieve superior tensile properties. Materials 11:146. https://doi.org/10.3390/ma11010146

Publisher's note Springer Nature remains neutral with regard to jurisdictional claims in published maps and institutional affiliations.